



Cite this: *Nanoscale*, 2018, **10**, 21353

## Transformation of carbon-supported Pt–Ni octahedral electrocatalysts into cubes: toward stable electrocatalysis†

Meital Shviro,<sup>†‡a</sup> Martin Gocyla,<sup>†‡a</sup> Roland Schierholz,<sup>†‡b</sup> Hermann Tempel,<sup>†‡b</sup> Hans Kungl,<sup>b</sup> Rüdiger-A. Eichel<sup>†‡b</sup> and Rafal E. Dunin-Borkowski<sup>a</sup>

Octahedral Pt–Ni catalyst nanoparticles (NPs) are predicted to exhibit high activity for the oxygen reduction reaction. However, until now this class of catalysts has been limited by its long-term performance, as a result of compositional and morphological instabilities of the NPs. *In situ* transmission electron microscopy (TEM) is a powerful technique for understanding morphological and compositional evolution under controlled conditions. It is of great importance to study the evolution of the morphology and elemental distribution in bimetallic NPs and their interaction with the support in reducing and oxidizing treatments at the atomic scale for the rational design of catalysts. Here, we use *in situ* TEM to follow dynamic changes in the NP morphology, faceting and elemental segregation under working conditions in previously unreported Pt–Ni core–shell octahedral structures. We follow changes in the Pt–Ni catalyst from a segregated structure to an alloyed shell configuration and then a more spherical structure as a function of temperature under reducing conditions. Exposure to an oxidizing environment then leads to oxidation of the C support, while the spherical NPs undergo a cycle of transformations into cubic NPs followed by the reaction to spherical NPs. The formation of the cubic NPs results from CO formation during C oxidation, before it is finally oxidized to CO<sub>2</sub>. Our observations may pave the way towards the design of optimized structure–stability electrocatalysts and highlight the importance of TEM visualization of degradation and transformation pathways in bimetallic Pt–Ni NPs under reducing and oxidizing conditions.

Received 25th July 2018,  
Accepted 14th October 2018  
DOI: 10.1039/c8nr06008h  
rsc.li/nanoscale

Pt–Ni octahedral nanoparticles (NPs) are an evolving class of electrocatalysts.<sup>1</sup> A strong focus has been placed on the control of the compositions, shapes and sizes of Pt–Ni based nanostructures, in order to improve their catalytic activities.<sup>2</sup> Although there have been many studies of Pt–Ni octahedral NPs with different compositions, sizes and activities for electrocatalysis, considerable work is still needed to optimize such catalysts due to their lack of durability. Previous work focused on the degradation of Pt–Ni octahedral NPs for the design of new catalysts.<sup>3</sup> The work inferred that the degradation process under electrochemical treatment was caused by the loss of

octahedral shape due to Ni dissolution from the {111} facets<sup>3</sup> or migration of Pt surface atoms.<sup>4</sup> Several approaches were used to try to suppress the degradation process. For example, it was attempted to prevent dissolution of Ni from the {111} facets by adding an ultrathin Pt layer to the Pt–Ni octahedra.<sup>5</sup> Doping of Pt–Ni octahedra with a third metal has also been used in the attempts to prevent degradation.<sup>4,6,7</sup> For example, Beermann *et al.*<sup>4</sup> doped Pt–Ni octahedra with Rh and suppressed the Pt migration on the surface. Theoretical calculations by Cao *et al.*<sup>8</sup> and Jia *et al.*<sup>9</sup> underlined the beneficial impact of adding a third metal. They predicted a limitation of the Ni dissolution rate resulting from a reduction in the Ni surface atom equilibrium concentration.<sup>8</sup>

Additional annealing treatments have been employed as a strategy to optimize the long-term catalytic behavior of Pt–M (M = transition metal) NPs by tuning their size, surface faceting and near-surface elemental distribution.<sup>10,11</sup> Enhanced catalytic performance was reported for annealed Pt–M NPs and correlated with the specific surface atomic configuration created during thermal annealing.<sup>11</sup> However, high temperature thermal annealing of shaped NPs can result in undesired morphological changes, as reported in transmission electron

<sup>a</sup>Ernst Ruska-Centre for Microscopy and Spectroscopy with Electrons, Forschungszentrum Jülich GmbH, 52425 Jülich, Germany.  
E-mail: m.shviro@fz-juelich.de

<sup>b</sup>Institute of Energy and Climate Research 9, Fundamental Electrochemistry, Forschungszentrum Jülich GmbH, 52425 Jülich, Germany

† Electronic supplementary information (ESI) available: (i) A text file with all experimental information and additional images recorded during *in situ* TEM measurements, and (ii) a video avi file showing the continuous formation and degradation of cubic shaped nanoparticles at 500 °C under oxidizing conditions. See DOI: 10.1039/c8nr06008h

‡ These authors contributed equally.

microscopy (TEM) studies of the thermal annealing of shaped Pt nanoparticles.<sup>10</sup> *In situ* TEM is increasingly used to study morphological stability and surface compositional evolution at the atomic scale under controlled working conditions, *e.g.*, in annealing environments. An *in situ* TEM study was performed on sandwich-like Pt–Ni octahedral NPs, which were transformed into Pt–Ni alloy octahedral NPs during mild thermal annealing at 200 °C under vacuum.<sup>12</sup> By using an *in situ* TEM holder based on a MEMS chip it was demonstrated that Pt-rich Pt–Ni octahedra underwent morphological changes including the formation of a thin Pt shell on their {111} facets.<sup>13</sup> By following this approach, we<sup>14</sup> tracked the morphological evolution as a function of temperature of Ni-rich Pt–Ni octahedra, for which the formation of a thin Pt shell on the {111} facets was accompanied by cuboctahedron formation. However, the *in situ* studies of the stability of Pt–Ni NPs during annealing treatments under a gas atmosphere have not yet been carried out in detail. In particular, the fact that most catalysts are stored in air may result in surface oxidation and consequent changes in both their surface structures (*e.g.*, dissolution of Pt and Ni atoms from vertex sites<sup>8</sup>) and their electronic properties,<sup>15</sup> resulting in a change in their catalytic activity. The oxidation behavior of a metallic alloy is further complicated by the presence of different cations, which may result in selective oxidation of one component of the alloy.<sup>16</sup>

Here, we study the morphological and compositional changes in a previously unreported Pt–Ni octahedral core-shell structure under working conditions. We perform *in situ* TEM annealing experiments both under vacuum (*i.e.*, under reducing conditions) and in the presence of an oxidizing gas atmosphere. In each case, we use high-angle annular dark field scanning TEM (HAADF STEM) and energy dispersive X-ray spectroscopy (EDX) to gain additional insight into the structure–stability relationship regarding morphology as well as elemental distribution. We follow MEMS chips for the dynamic evolution of NP morphology, faceting and elemental segregation under working conditions under  $1 \times 10^{-10}$  bar vacuum and 1.1 bar O<sub>2</sub>. We establish not only a consistent picture of the structure–stability relationship of this C-supported Pt–Ni core-shell octahedral structure, but also infer from *in situ* TEM that CO is an intermediate state during C oxidation accompanied by the unprecedented transformation into cubes in the presence of O<sub>2</sub> and thermal energy.

## Results and discussion

Pt–Ni octahedral NPs were prepared using a previously unreported synthesis pathway using benzyl alcohol (BA) as the solvent at 150 °C as described in the experimental part of the ESI†. Different shapes of Pt–Ni NPs were obtained by this method, 70% of which had octahedral shapes, with a broad size distribution (Fig. S1G in the ESI†). TEM images of the octahedral structures (Fig. S1A in the ESI†) reveal a vertex-to-vertex particle size along the <100> directions of 16

± 2 nm. The HAADF STEM image shown in Fig. S1B† highlights the fact that this NP is a truncated octahedron viewed approximately along <110> with flat {111} facets and truncated vertices that take the form of {100} facets. The corresponding EDX maps shown in Fig. S1C–E† reveal a segregated structure with a Pt-rich shell and a Ni-rich core. The interpretation of our experimental EDX result is consistent with the simulated EDX maps for Pt–Ni core-shell octahedra from previous work.<sup>17</sup> The HAADF STEM image shows a consistent bright stripe around the outer part of the NP, while the core is less bright. The presence of oxygen at the surface/subsurface regions is assigned to the initially prepared octahedral NPs due to their exposure to air after preparation and is seen in the C-supported Pt–Ni core-shell octahedra in the EDX map in Fig. S1F†.

This structural observation has not previously been reported for Pt–Ni octahedra. Previous work has focused on the growth mechanism for different synthetic pathways of octahedral NPs with different Pt and Ni distributions.<sup>18–20</sup> Furthermore, a segregated structure was reported with Pt forming a hexapod structure with six arms along the <100> directions, while Ni was deposited on the {111} faces<sup>18</sup> and an octahedral structure, with Pt distributed along three orthogonal Cartesian axes and at the NP edges, while Ni filled the {111} faces.<sup>19</sup> Recently, a Pt core in a Pt–Ni alloy shell octahedral structure has been found.<sup>20</sup> In contrast, the structure presented here has not, to the best of our knowledge, yet been described in the studies of PtNi octahedra.

We studied the stabilities of our Pt–Ni core-shell octahedra first by performing *in situ* heating in the TEM under reducing conditions (see the ESI†). Fig. 1 shows high-resolution TEM (HRTEM) images at elevated temperatures of a representative Pt–Ni octahedral NP during annealing at temperatures between 50 °C and 600 °C. The Pt–Ni octahedral structure shows no visible morphological changes up to 300 °C (Fig. 1A–F). Above 300 °C, it begins to change its shape. The edges start to become rounder, as do the originally flat {100} facets (Fig. 1G). Such a rounding of the octahedral structure is consistent with the previous work.<sup>13,14</sup> On increasing the temperature to 500 °C, the original octahedral shape was still visible (Fig. 1J). A transition to a fully spherical shape was observed at 600 °C (Fig. 1L). Fig. S2 in the ESI† shows additional HRTEM images, which display a similar behavior.

The Pt–Ni octahedral NP shows Moiré fringes with a spacing of 0.4–0.49 nm in the core region up to 300 °C. The arrows in Fig. S3A† mark a Moiré fringe spacing of 0.49 nm. With increasing temperature, the spacing distance of the Moiré fringes in the core region increased to 2.00–2.07 nm at 400 °C. The arrows in Fig. S3B† mark a Moiré fringe spacing of 2.07 nm. The Moiré fringes disappear above a temperature of 500 °C.

Two overlapping materials with different lattice parameters and/or a relative rotation angle lead to the formation of Moiré fringes. She *et al.*<sup>21</sup> described the appearance of Moiré fringes in Au–Ni core-shell nanoparticles due to the difference in the crystalline plane spacing between the Au core and the Ni shell.

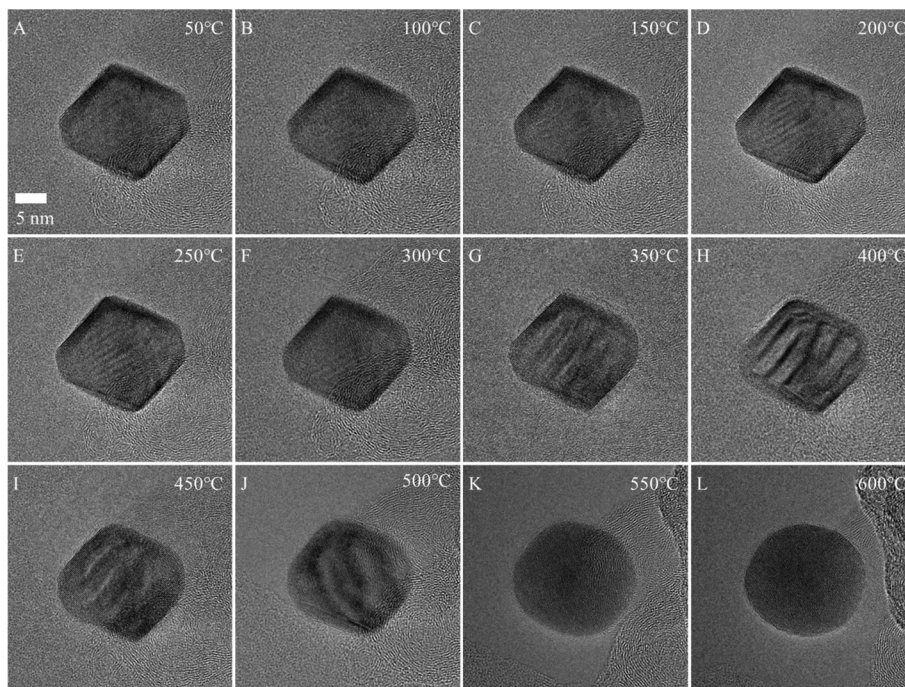


Fig. 1 HRTEM images of Pt–Ni octahedral NPs recorded during *in situ* thermal annealing at elevated temperature under vacuum between 50 °C and 600 °C.

The Moiré fringe spacing  $d$  was calculated using the expression:

$$d = \frac{d_2 \times d_1}{(d_2 - d_1)}, \quad (1)$$

where  $d_1$  and  $d_2$  correspond to the lattice spacings of the two materials. A similar calculation for Pt {111} planes (0.23 nm) and PtO<sub>2</sub> {111} planes (0.15 nm), Ni {111} planes (0.20 nm) and PtO<sub>2</sub> {111} planes (0.15 nm), and NiO {111} planes (0.24 nm) and PtO<sub>2</sub> {111} planes (0.15 nm) leads to Moiré fringe spacings of 0.5, 0.4 and 0.36 nm, respectively. These values are close to the experimental values of 0.4–0.49 nm for the Moiré fringe spacings below 300 °C and could therefore be attributed to the difference in the crystalline plane spacing between a PtO<sub>2</sub> surface layer and Pt, Ni and/or NiO inside the NPs. The presence of an oxide is consistent with the EDX map of the pristine material shown in Fig. S1F.† An enrichment of O at the edges is also seen in EDX line scans recorded from Pt–Ni core–shell octahedra at 300 °C (marked by arrows in Fig. S4†).

A calculation for NiO {111} planes (0.24 nm) and Pt–Ni {111} planes (0.22 nm) leads to a Moiré fringe spacing of 2.08 nm. At temperatures higher than 300 °C, this value is close to the experimental Moiré fringe spacing of 2.00–2.07 nm and could therefore be attributed to the formation of a Pt-rich region alloyed with Ni in the outer part of the NPs and a NiO core region. EDX line scans recorded from the NP after annealing at 500 °C suggest the formation of a NiO core region, as they show a more homogeneous O distribution when compared to the O enrichment visible at the edges of the NP at 300 °C (Fig. S4†).

The pristine Pt–Ni NP has a clear segregated structure with a Pt-rich shell and a Ni-rich core (Fig. S1†). In order to study the effect of annealing on the local composition, we recorded EDX maps alongside HAADF STEM images. (1) Up to 300 °C, no compositional changes are observed: Pt and Ni are clearly separated from each other in the EDX maps (Fig. 2D, G and J), in agreement with the lower intensity in the core and higher intensity in the outer part of the NP in the HAADF STEM image shown in Fig. 2A. (2) The local compositions in the Pt–Ni octahedra changed slightly when the temperature reached 500 °C. As described above, at 500 °C, the corners started to become rounder and the local composition started to change. Interdiffusion of Pt and Ni occurred, with Pt from the shell diffusing into the inner part of the NP (Fig. 2B, E, H and K), resulting in a thicker Pt-rich region alloyed with Ni (marked using arrows in Fig. 2K) and a smaller Ni core (Fig. 2K). This conclusion is consistent with the decrease in contrast variation in the HAADF STEM image shown in Fig. 2B compared to Fig. 2A and is in line with the appearance of Moiré fringes with interval distances between 2.00 and 2.07 nm at a temperature higher than 300 °C as described above.

This morphological and compositional evolution is similar to that observed for the smaller octahedral nanoparticles (Fig. S5 in the ESI†).

This process is described in terms of the movement of Ni towards the surface by the replacement of Pt in PtO<sub>x</sub> species by Ni due to its higher oxygen affinity.<sup>22</sup> A proposed Pt-rich surface with subsurface Ni after annealing<sup>13,14</sup> is in line with our present results. The experimental work by Stamenkovic *et al.*<sup>23</sup> on Pt<sub>3</sub>–Ni {111} alloy surfaces demonstrated superior

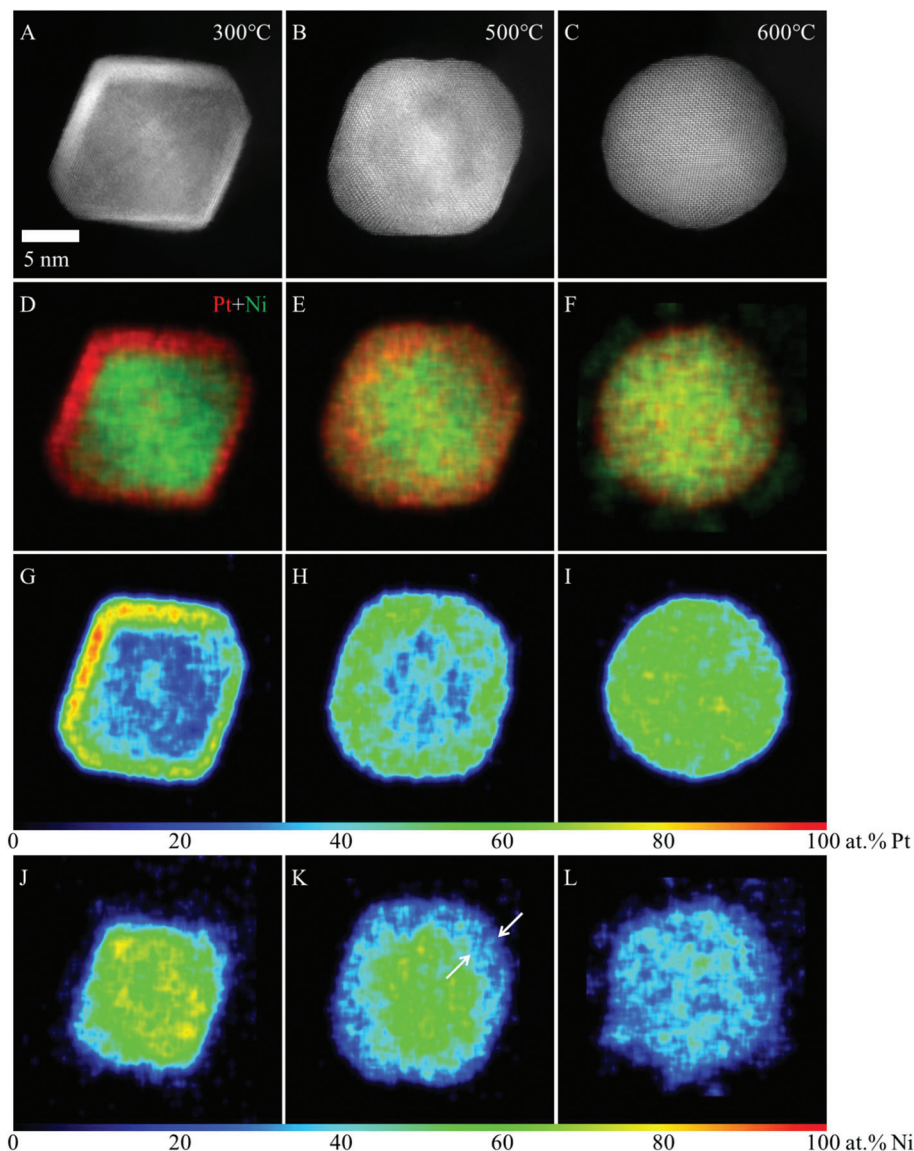


**Fig. 2** HAADF STEM images and EDX composition maps of a Pt–Ni octahedral nanoparticle. The high-resolution HAADF STEM image of a nanoparticle oriented close to (110) after annealing at (A) 300 °C, (B) 500 °C, and (C) 600 °C. (D–F) Corresponding Pt (red) and Ni (green) signals in qualitative EDX composition maps. (G–I) and (J–L) Corresponding quantitative EDX composition maps for (G–I) Pt and (J–L) Ni, according to the color legends included below the figures. Arrows in (K) mark the resulting Pt-rich region alloyed with Ni after 500 °C.

catalytic behavior for the ORR compared to pure Pt surfaces and was theoretically supported by the work of Duan *et al.*<sup>24,25</sup> Pan *et al.* reported surface Ni enrichment after annealing their octahedra, accompanied by an increase in the ORR activity.<sup>12</sup> The octahedra in the present study could be tuned between high activity and long-term stability by thermal annealing, whereas the initially thick Pt shell could lower the ORR activity as it was shown that pure Pt surfaces are less active than Pt–Ni surfaces;<sup>23,24,26</sup> a very thin Pt shell with a Ni subsurface could decrease the durability of the catalyst due to Ni dissolution under electrochemical conditions.<sup>3</sup> A compromise in shell thickness after annealing would result in a valuable long-term catalyst.

The use of a high temperature results in an undesired morphological shape, as shown elsewhere.<sup>10,12–14</sup> In the present study, after annealing at 600 °C the octahedral shape is no longer retained; the HAADF STEM image (Fig. 2C) shows no contrast variation between the shell and the core, the Moiré fringes disappear and in the EDX maps an alloyed structure is observed due to further interdiffusion of Pt and Ni with increasing temperature.

The average composition of the octahedral particles at 300, 500, and 600 °C is Pt 62 at%, Ni 38 at%; Pt 69 at%, Ni 31 at%; and Pt 75 at%, Ni 25 at%, respectively (Fig. S6A†). Hence, Ni dissolution takes place during the heating process. In order to study the Ni dissolution under reducing conditions in more

detail, large irregular C-supported Ni-rich Pt–Ni NPs were analyzed before and after annealing at 800 °C under reducing conditions. The overall composition of larger NPs in the initial state, shown in Fig. S7A–E†, is Pt 3 at%, Ni 97 at%. After annealing under vacuum at 800 °C, only Pt-rich cores remain, while little Ni is left (Fig. S7F–J†). Therefore, at a higher temperature, the dissolution of Ni also takes place for large C-supported irregular Ni-rich Pt–Ni nanoparticles. A volatile Ni-containing species is likely to be formed during this process. In order to investigate the role of the C support, Pt–Ni nanoparticles without a C support were also analyzed (Fig. S8†). Without a C support, the Pt–Ni nanoparticles, in both their initial state and after annealing at 500 °C under reducing conditions, had a measured composition of Pt 21 at%, Ni 79 at% (Fig. S6C†). Therefore, no Ni dissolution takes place for Pt–Ni nanoparticles without a C support. In contrast, in Pt–Ni C-supported NPs, a volatile Ni and C containing species is likely to be formed.

This process, which is referred to as the carbothermal reduction of metal oxides, may be associated with several possible mechanisms that have been discussed in the literature.<sup>27–29</sup> For Pt–Ni core–shell octahedral NPs, Ni is thought to move towards the surface of the octahedral NPs through exchange with Pt in PtO<sub>x</sub> species, thus forming NiO, as described above. The NiO can then react with the C support to form a Ni-species vapor. Gaseous Ni-species can be extracted by the ion getter pumps of the TEM before their condensation can lead to the formation of Ni-rich NPs on the substrate or volatile Ni-species condensate inside the TEM elsewhere outside the field of view. The initial decomposition temperature of 500 °C for nanoscale carbothermal reduction inferred from the present study is lower than the decomposition temperatures reported in the literature, which are typically between 600 and 772 °C.<sup>29</sup> We assume that this discrepancy may be attributed to the smaller particle size in the present work and to the influence of the high energy electron beam in the TEM.

The reduction of NiO by C is, in contrast to its thermal dissociation, thermodynamically favored.<sup>30</sup> The reduction of NiO by C should therefore occur at lower temperatures, which may explain the present results for Pt–Ni NPs without a C support, where Ni is not lost at 500 °C. Furthermore, L'vov<sup>29</sup> suggested a mechanism whereby NiO dissociates into gaseous Ni and O<sub>2</sub>, but Ni immediately condenses, which may provide another explanation for why no Ni dissolution takes place for Pt–Ni NPs without C support at 500 °C.

After investigating the Pt–Ni core–shell octahedra during annealing under reducing conditions, the same Pt–Ni core–shell octahedra were examined during annealing under oxidizing conditions with an annealing treatment. The Pt–Ni NPs were deposited on a MEMS chip, which was placed in a gas reaction specimen holder that was loaded with 1.1 bar of O<sub>2</sub>. Below 300 °C, in the absence of gas, no changes were visible. Therefore, any change taking place in this temperature range can be attributed to the presence of oxygen. After 30 min at 250 °C, no change in the Pt–Ni octahedral NPs was visible.

However, in C black began the formation of a discontinuous C structure (Fig. 3B). Fig. S9† illustrates the development of the morphology of a C black particle in 1.1 bar of oxygen gas recorded at 23, 250 and 500 °C, respectively. As mentioned above, the primary C black particle became partly hollow (marked using arrows in Fig. S9B†) at 250 °C, before a bigger discontinuous C structure developed at 500 °C (marked using arrows in Fig. S9C†). The final structure in Fig. S9D† shows only a small amorphous skin.

A change in C black under oxidizing conditions was previously reported by Burden *et al.*,<sup>31</sup> who used a gas flow of 20 mbar and observed gaseous products of CO and CO<sub>2</sub>, as well as the formation of a shell after 450 s, with the inner material separating from the walls.<sup>31</sup> In line with our result, they<sup>31</sup> observed in detail that the C black structure became amorphous and hollowed out before an amorphous skin remained in the final structure.

At 500 °C, no significant change to the Pt–Ni octahedral-shaped NP had been observed under vacuum. In contrast, on heating the sample to 500 °C in O<sub>2</sub>, the Pt–Ni octahedra transformed into cubic structures (blue circles in Fig. 3C and D), which then transformed continuously between spherical and cubic shapes until the C was consumed. Fig. 4 shows TEM images recorded at 500 °C of representative NPs transforming into cubic structures during annealing in 1.1 bar. The NP in Fig. 4A (in the blue circle) has a cuboid structure with edge lengths of 14 and 9 nm. This cuboid NP transforms into a spherical NP (blue circle in Fig. 4B) and undergoes several oscillations between spherical and cubic shapes (Fig. 4C–F). A similar oscillation is shown for a different NP in Fig. 4G–L (in the red circle). More complex transformation pathways are also observed (Fig. 4M–X). For instance, a cubic NP with a 10 nm edge length and a non-cubic NP (Fig. 4M) approach each other (Fig. 4N) and then coalesce (Fig. 4O). The resulting NP transforms into a cubic NP with a 20 nm edge length (Fig. 4P), before it starts to split (Fig. 4Q) into a non-cubic NP and an L-shaped NP (Fig. 4R). The L-shaped NP starts to split further (Fig. 4S–U), before two non-cubic NPs are formed (Fig. 4V). One of the NPs transforms into a cuboid structure (Fig. 4W, right NP) and then into an L-shaped NP. The dynamics of the transformations can be seen in a video in the ESI.† The mechanism of C oxidation to CO<sub>2</sub> can be accompanied by the formation of CO.<sup>32,33</sup> The previous work<sup>31</sup> suggested the formation of CO from C black only as a result of electron beam irradiation of oxygen as mentioned above. Here, the formation of CO is supported by additional heating.

Previous studies revealed that CO selectively adsorbs onto Pt {100} crystal facets.<sup>34</sup> CO then stabilizes the {100} surfaces and plays a key role in the formation of Pt and Pt–M nanocubes.<sup>35–38</sup> The Pt–Ni core–shell octahedra examined during annealing under inert conditions, with an annealing treatment at 500 °C, do not transform into cubic structures and more than an amorphous C skin remains from the C black structure (Fig. S10†).

In order to confirm the formation of a C containing gas during annealing of the C-black-supported Pt–Ni NPs under an

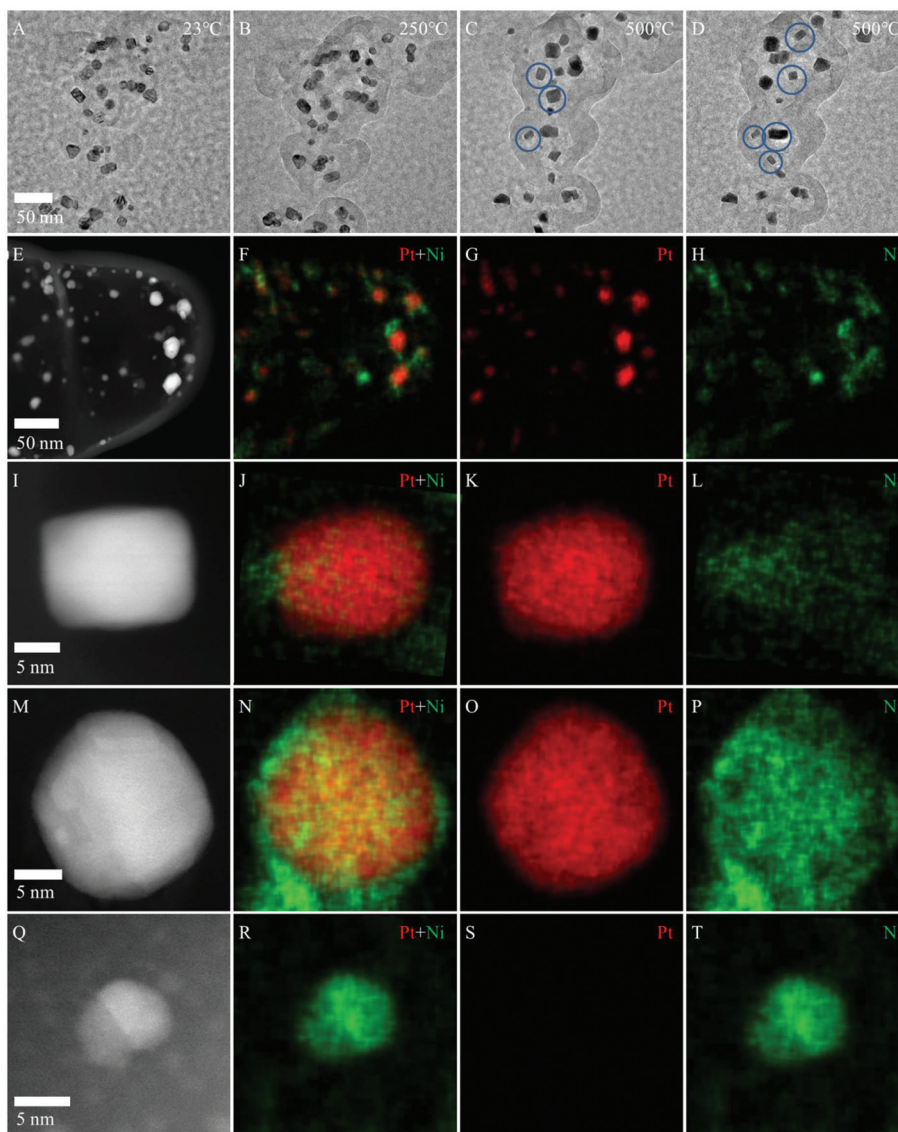


**Fig. 3** (A–D) Bright-field TEM images recorded at (A) room temperature, (B) 250 °C and (C and D) 500 °C in 1.1 bar of oxygen. (E, I, M, and Q) HAADF STEM images of the NPs after heating at 500 °C in 1.1 bar of oxygen. (F–H, J–L, N–P and R–T) Corresponding EDX maps showing Pt (red) and Ni (green).

oxygen atmosphere, thermal gravimetric analysis (TGA) coupled with mass spectrometry (MS) was carried out. An increase in an ion current was visible for a mass-to-charge ratio of 44 ( $\text{CO}_2$ ) between 350 °C and 500 °C as a result of the production of  $\text{CO}_2$ , as shown in Fig. 5. A significant signal for CO production was not apparent, due to only local enrichment of CO and fast further oxidation to  $\text{CO}_2$ .

These observations are in agreement with the continuous destruction and reformation of the cubic shapes, with a concentration of local CO leading to the formation of cubes, followed by non-cubic structures as soon as CO was oxidized to  $\text{CO}_2$ . The fundamental related question is whether CO is an intermediate in  $\text{CO}_2$  formation, or whether  $\text{CO}_2$  is produced directly from C.<sup>39</sup> Our observation of the formation of Pt–Ni nanocubes, followed by degradation to shapeless NPs, suggests

that the formation of CO is an intermediate step in C oxidation, which has not previously been inferred from *in situ* TEM measurements (see the video in the ESI†).

Fig. 3E–T show the HAADF STEM images and corresponding EDX maps of the products. The overview EDX maps in Fig. 3F–H reveal both Pt-rich and Ni-rich NPs. Higher magnification images in Fig. 3I–L reveal a cubic NP with rounded corners, which consists mainly of Pt, with a small amount of Ni surrounding the cube.

$\text{CO}$ -assisted wet chemistry synthesis of cubes is known to result in round corners,<sup>38</sup> as observed here.

For spherical NPs that were formerly cubes, a similar Pt and Ni distribution is visible (Fig. 3O–P). The NP imaged in Fig. 3M–P consists mainly of Pt, while Ni is only attached on its outer part. Ni dissolution in the form of a volatile Ni- and

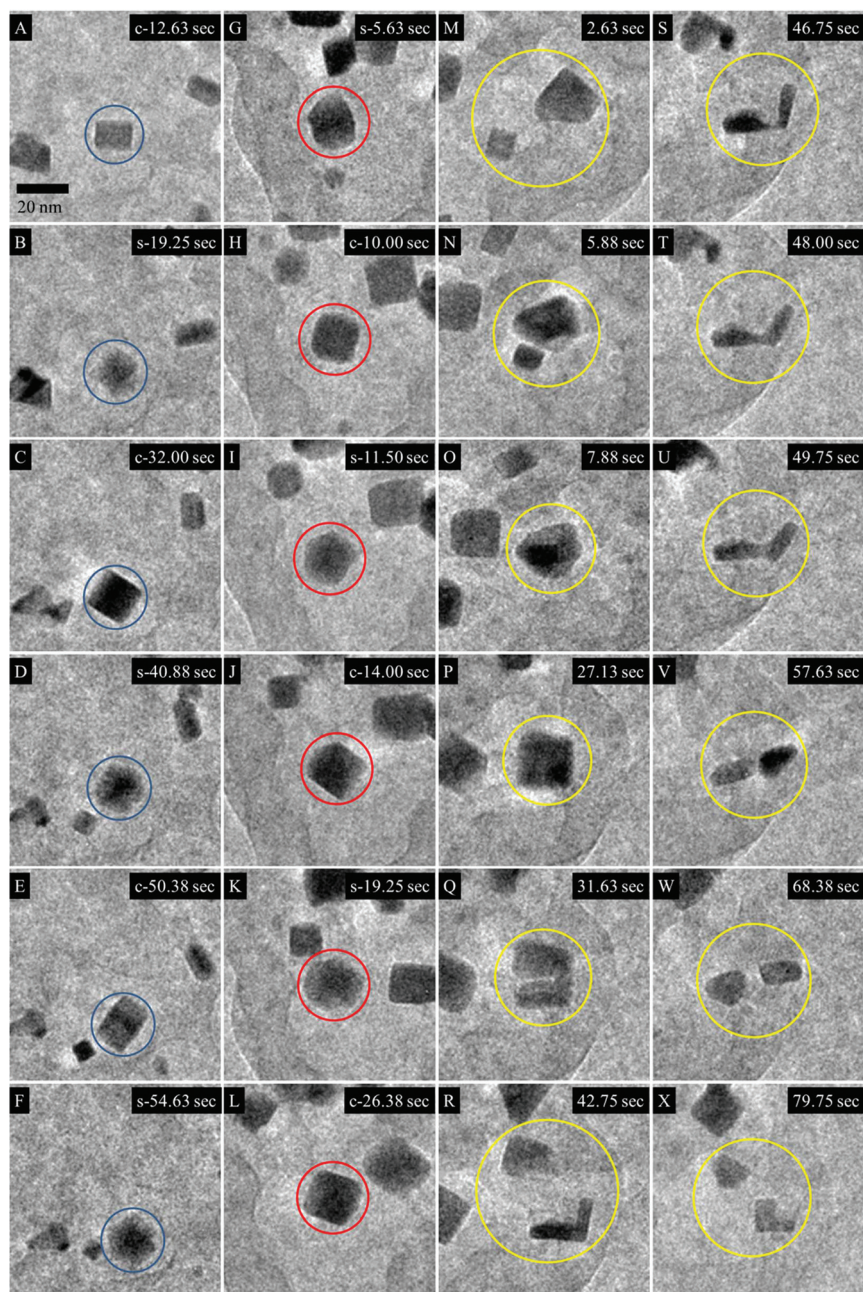


**Fig. 4** (A–X) Bright-field TEM images recorded at 500 °C in 1.1 bar of oxygen showing transformation pathways between spherical and cubic shapes. (A–F) Blue, (G–L) red and (M–X) yellow circles mark identical nanoparticles. The actual time is given in seconds (s). The symbols c and s mark the particles that are obviously cubic or spherical, respectively. Further details are provided in the text.

C-based compound was not only observed here, but also to a smaller extent under reducing conditions. However, pure Ni NPs were formed in addition to Pt-rich NPs under oxidizing conditions (see Fig. 3Q–T).

The NPs that formed by the TGA-MS measurement were analyzed using HAADF STEM imaging and EDX, as shown in Fig. 5. The images reveal Pt-rich NPs, with Ni attached only on their outer parts (Fig. 5B and C), as well as Ni-rich NPs (Fig. 5D and E), supporting the results obtained

after *in situ* measurement under an oxygen atmosphere at 500 °C.

Diffusion of Ni towards NP surfaces at higher temperatures in oxygen was already reported for a different octahedral structure.<sup>22</sup> The surface Ni could then react with the formed CO to produce Ni(CO)<sub>4</sub>. Heinicke<sup>40</sup> reported that Ni(CO)<sub>4</sub> formation was inhibited in the presence of oxygen. However, as soon as a Ni surface site was not covered by oxygen, the reaction could take place. In the present study, CO was formed while the NPs

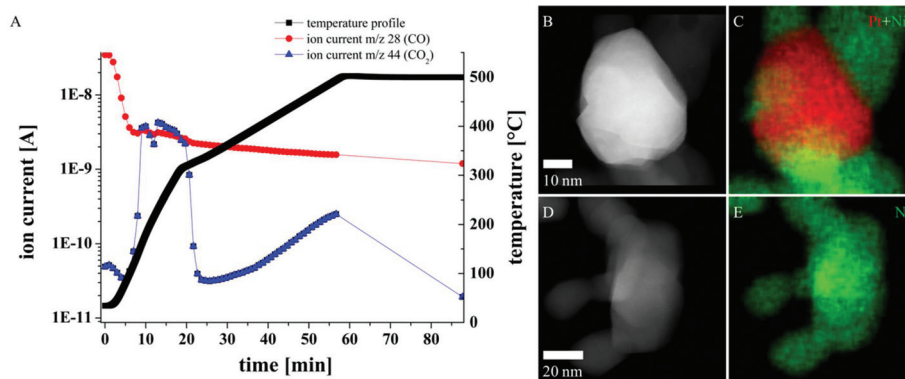


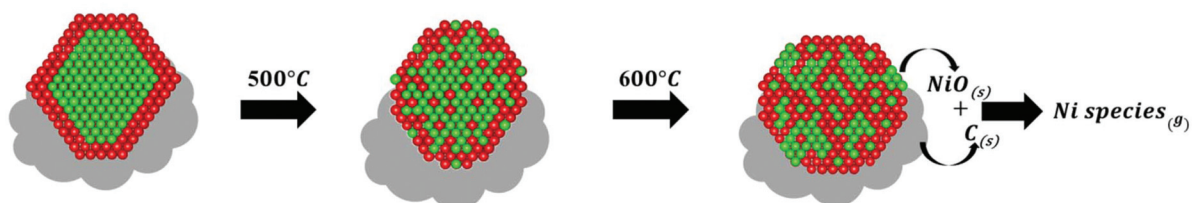
**Fig. 5** (A) Time-dependent temperature profile and ion current release for a mass of 28 (CO) and 44 (CO<sub>2</sub>) during TGA-MS measurement under an oxygen atmosphere. (B and D) HAADF STEM images of NPs after TGA-MS and (C and E) corresponding EDX maps showing Pt (red) and Ni (green).

simultaneously detached from the support, leading to a dynamic situation, in which some Ni could not be covered by oxygen and could react with CO. The decomposition of volatile Ni(CO)<sub>4</sub> into Ni and CO is well known from previous work.<sup>41</sup> This behavior is supported by the formation of Ni NPs (*e.g.*, Fig. 3Q–T), while the presence of CO is suggested indirectly by the cube formation. It should, however, be noted that the mere coexistence of CO and Ni does not automatically lead to the formation of Ni(CO)<sub>4</sub>.<sup>42–44</sup> Although a fully reduced Ni surface species may be available for the formation of Ni(CO)<sub>4</sub>, the pres-

ence of a reducing gas and thermodynamically favored conditions (a temperature below 150 °C) are missing in our experimental environment.<sup>42</sup> Therefore, in the present study, the Ni-rich NP formation most likely results from Ni diffusion towards an oxygen-rich environment.

Based on the present *in situ* study, Fig. 6 illustrates a proposed morphological evolution sequence for the transformation of octahedral NPs under reducing (Fig. 6A) and oxidizing (Fig. 6B) conditions. In both the cases, the starting materials are core-shell octahedral NPs.

#### A inert condition: $\Delta T$ + vacuum



#### B oxidizing condition: $\Delta T$ + O<sub>2</sub>

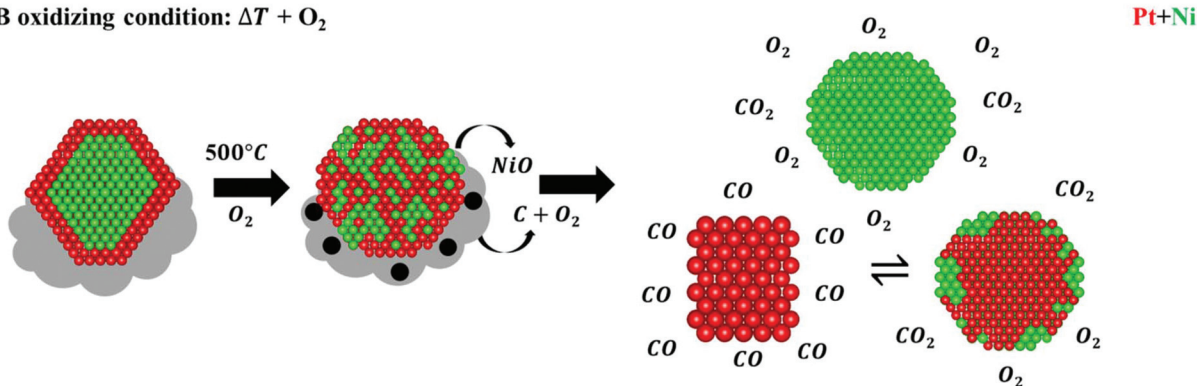


**Fig. 6** Schematic diagrams illustrating the proposed morphological evolution of Pt–Ni core-shell octahedral NPs with Pt (red) and Ni (green) distributions during (A) *in situ* thermal heating and (B) *in situ* thermal heating in oxygen. Further details are provided in the text.

Under reducing conditions, the core-shell octahedral NPs form a more alloyed octahedral structure above 300 °C, with Ni close to their surfaces. When the temperature is increased to 600 °C, the octahedral structure is lost, in favor of a spherical structure. With increasing temperature, the dissolution of Ni is visible; Ni-rich NPs are not observed to form on the support. The formation of NiO by the exchange with PtO<sub>x</sub> species leads to the carbothermal reduction of NiO. Under inert conditions, the resulting volatile Ni-species and CO are likely to be extracted by the ion getter pumps of the TEM before the condensation of Ni-rich NPs can occur.

Under oxidizing conditions at 500 °C, Pt-rich cubic NPs, spherical Pt-rich NPs with attached Ni and Ni-rich NPs are formed. The Ni NPs probably form as a result of the diffusion of Ni due to its high affinity for oxygen, whereas C is oxidized to CO and CO<sub>2</sub>; the resulting CO is absorbed onto the Pt, which in turn forms a cubic shape. Once the CO is further oxidized to CO<sub>2</sub>, the Pt cubes are destroyed and spherical NPs form as soon as the local environment is rich in O<sub>2</sub> and/or CO<sub>2</sub>.

In conclusion, we have performed *in situ* TEM thermal annealing of previously unreported Pt-Ni octahedral NPs supported on carbon under reducing and oxidizing conditions up to 600 °C. The previously unreported core-shell Pt-Ni octahedra maintain their shapes over a wide temperature range (up to 500 °C) under reducing conditions, although the starting core-shell structure becomes more alloyed due to the interdiffusion of Pt and Ni, leading finally to an alloyed spherical Pt-Ni structure. In contrast, under oxidizing conditions, the core-shell Pt-Ni octahedra maintain their shape over a narrower temperature range (below 500 °C). A transformation of the starting octahedral NPs to cubes was visible through the formation of CO. Its further oxidation to CO<sub>2</sub> leads to the formation of spherical NPs in a continuous process, until all of the C is consumed. The results reveal the ability to tune the optimal structure-stability relationship of the core-shell octahedral Pt-Ni NPs as an electrocatalyst. They also address the fundamental role of CO as an intermediate stage during carbon oxidation. This study introduces a methodology of degradation and transformation pathways for various nanomaterials including shaped NPs, core-shell NPs and Janus NPs.

## Author contributions

M. S. and M. G. initiated the idea, designed the experiments, synthesized the material, performed the *in situ* HRTEM/STEM experiments, processed the experimental data, interpreted the data and drafted the manuscript. H. T. performed the TGA-MS measurement. All the authors participated in the scientific discussions and wrote the manuscript.

## Conflicts of interest

There are no conflicts to declare.

## Acknowledgements

Financial support was provided by the Deutsche Forschungsgemeinschaft (DFG) grant HE 7192/1-1. M. G. thanks Werner Pieper, Rolf Speen, Robert Nijland and Jie Xu for technical support. M. S. thanks the Alexander von Humboldt Foundation for financial support. The *in situ* gas reaction heating holder (DENSSolutions B. V.) was funded by the Helmholtz Energy Materials Foundry (HEMF).

## References

- 1 P. Strasser, *Science*, 2015, **349**, 379–380.
- 2 M. Heggen, M. Gocyla and R. E. Dunin-Borkowski, *Adv. Phys.: X*, 2017, **2**, 281–301.
- 3 C. Cui, L. Gan, M. Heggen, S. Rudi and P. Strasser, *Nat. Mater.*, 2013, **12**, 765–771.
- 4 V. Beermann, M. Gocyla, E. Willinger, S. Rudi, M. Heggen, R. E. Dunin-Borkowski, M. G. Willinger and P. Strasser, *Nano Lett.*, 2016, **16**, 1719–1725.
- 5 J. Park, J. Liu, H. C. Peng, L. Figueroa-Cosme, S. Miao, S. Il Choi, S. Bao, X. Yang and Y. Xia, *ChemSusChem*, 2016, **9**, 2209–2215.
- 6 X. Huang, Z. Zhao, L. Cao, Y. Chen, E. Zhu, Z. Lin, M. Li, A. Yan, A. Zettl, Y. M. Wang, X. Duan, T. Mueller and Y. Huang, *Science*, 2015, **348**, 1230–1234.
- 7 L. Bu, Q. Shao, B. E. J. Guo, J. Yao and X. Huang, *J. Am. Chem. Soc.*, 2017, **139**, 9576–9582.
- 8 L. Cao and T. Mueller, *Nano Lett.*, 2016, **16**, 7748–7754.
- 9 Q. Jia, Z. Zhao, L. Cao, J. Li, S. Ghoshal, V. Davies, E. Stavitski, K. Attenkofer, Z. Liu, M. Li, X. Duan, S. Mukerjee, T. Mueller and Y. Huang, *Nano Lett.*, 2018, **18**, 798–804.
- 10 Z. L. Wang, J. M. Petroski, T. C. Green and M. a. El-Sayed, *J. Phys. Chem. B*, 1998, **102**, 6145–6151.
- 11 C. Wang, G. Wang, D. van der Vliet, K.-C. Chang, N. M. Markovic and V. R. Stamenkovic, *Phys. Chem. Chem. Phys.*, 2010, **12**, 6933–6939.
- 12 Y.-T. Pan, J. Wu, X. Yin and H. Yang, *AIChE J.*, 2016, **62**, 399–407.
- 13 L. Gan, M. Heggen, C. Cui and P. Strasser, *ACS Catal.*, 2016, **6**, 692–695.
- 14 M. Gocyla, S. Kuehl, M. Shviro, H. Heyen, S. Selve, R. E. Dunin-Borkowski, M. Heggen and P. Strasser, *ACS Nano*, 2018, **12**, 5306–5311.
- 15 V. Stamenkovic, B. S. Mun, K. J. J. Mayrhofer, P. N. Ross, N. M. Markovic, J. Rossmeisl, J. Greeley and J. K. Nørskov, *Angew. Chem., Int. Ed.*, 2006, **45**, 2897–2901.
- 16 C.-M. Wang, A. Genc, H. Cheng, L. Pullan, D. R. Baer and S. M. Bruemmer, *Sci. Rep.*, 2014, **4**, 3683.
- 17 K. E. MacArthur, M. Heggen and R. E. Dunin-Borkowski, *Adv. Struct. Chem. Imaging*, 2018, **4**, 2.
- 18 L. Gan, C. Cui, M. Heggen, F. Dionigi, S. Rudi and P. Strasser, *Science*, 2014, **346**, 1502–1506.

- 19 A. Oh, H. Baik, D. S. Choi, J. Y. Cheon, B. Kim, H. Kim, S. J. Kwon, S. H. Joo, Y. Jung and K. Lee, *ACS Nano*, 2015, **9**, 2856–2867.
- 20 Q. Chang, Y. Xu, Z. Duan, F. Xiao, F. Fu, Y. Hong, J. Kim, S.-I. Choi, D. Su and M. Shao, *Nano Lett.*, 2017, **17**, 3926–3931.
- 21 H. She, Y. Chen, X. Chen, K. Zhang, Z. Wang and D.-L. Peng, *J. Mater. Chem.*, 2012, **22**, 2757–2765.
- 22 M. Ahmadi, F. Behafarid, C. Cui, P. Strasser and B. R. Cuenya, *ACS Nano*, 2013, **7**, 9195–9204.
- 23 V. R. Stamenkovic, B. Fowler, B. S. Mun, G. Wang, P. N. Ross, C. A. Lucas and N. M. Markovic, *Science*, 2007, **315**, 493–497.
- 24 Z. Duan and G. Wang, *J. Phys. Chem. C*, 2013, **117**, 6284–6292.
- 25 D. Gardini, J. M. Christensen, C. D. Damsgaard, A. D. Jensen and J. B. Wagner, *Appl. Catal., B*, 2016, **183**, 28–36.
- 26 Z. Duan and G. Wang, *Phys. Chem. Chem. Phys.*, 2011, **13**, 20178.
- 27 L. Gruner, *Traité de métallurgie generale*, Paris, 1875.
- 28 G. Tammann and A. Sworykin, *Z. Anorg. Allg. Chem.*, 1928, **170**, 62–70.
- 29 B. V. L'vov, *Thermochim. Acta*, 2000, **360**, 109–120.
- 30 B. V. L'vov, *Spectrochim. Acta, Part B*, 1989, **44**, 1257–1271.
- 31 A. P. Burden and J. L. Hutchison, *Carbon*, 1997, **35**, 567–578.
- 32 A. N. Hayhurst and M. S. Parmar, *Chem. Eng. Sci.*, 1998, **53**, 427–438.
- 33 P. L. Walker, R. L. Taylor and J. M. Ranish, *Carbon*, 1990, **29**, 411–421.
- 34 M. Chen, B. Wu, J. Yang and N. Zheng, *Adv. Mater.*, 2012, **24**, 862–879.
- 35 B. Wu, N. Zheng and G. Fu, *Chem. Commun.*, 2011, **47**, 1039–1041.
- 36 Y. Wang, Z. Sun, A. Kumbhar, Z. Luo, C. Wang, J. Zhang, N. Porter, C. Xu, K. Sun, B. Martens and J. Fang, *Chem. Commun.*, 2013, **49**, 3955–3957.
- 37 J. Wu, A. Gross and H. Yang, *Nano Lett.*, 2011, **11**, 798–802.
- 38 Y. Wu, S. Cai, D. Wang, W. He and Y. Li, *J. Am. Chem. Soc.*, 2012, **134**, 8975.
- 39 C. Li and T. C. Brown, *Carbon*, 2001, **39**, 725–732.
- 40 G. Heinicke, *Z. Anorg. Allg. Chem.*, 1963, **324**, 173–184.
- 41 A. Mittasch, *Z. Phys. Chem.*, 1902, **40U**, 1.
- 42 K. Lascelles, L. G. Morgan, D. Nicholls and D. Beyersmann, *Ullmann's Encycl. Ind. Chem*, 2000.
- 43 U. Ilya, E. Robert and T. Andreas, *Radiochim. Acta*, 2016, **104**, 531.
- 44 A. Morrison, J. J. Leitch, G. Szymanski, G. Moula, B. Barlow, I. J. Burgess, B. Shobeir, H. Huang and J. Lipkowski, *Electrochim. Acta*, 2018, **260**, 684–694.